Наносистеми, наноматеріали, нанотехнології
Nanosistemi, Nanomateriali, Nanotehnologii
2026, т. 24, № 2, сс. 549–563
https://doi.org/10.15407/nnn.24.02.0549

PACS numbers: 61.05.cp, 61.46.Hk, 61.66.Fn, 78.30.Hv, 78.40.Ha, 81.07.Bc, 81.20.Fw

Particle-Size Calculation for Synthesis of $ZnSO_4$ Nanoparticles Doped with Transition-Metal Ions

Ahmed Kadari and Yassine Sarir

Faculty of Matter Sciences,
Department of Chemistry,
University of Tiaret,
14000 Tiaret, Algeria

In the present work, we report the successful synthesis of zinc sulphate ($ZnSO_4$) nanoparticles (NPs) using the sol–gel processing. Zinc acetate is served as the precursor, while $Co(NO_3)_2$, $Cr(NO_3)_3$ and $Fe(NO_3)_3$ are used to achieve different doping levels. The synthesis involves the hydrolysis and gelation process, followed by the controlled evaporation of the solvent to facilitate the formation of $ZnSO_4$ NPs. The synthesized $ZnSO_4$ NPs are characterized, using various techniques, including XRD method and FT-IR spectroscopy to confirm their crystalline structure. UV–Vis spectroscopy is conducted to analyze the optical properties, revealing significant modifications in band-gap energy. Detailed analysis of crystallite sizes (D) is presented. Average crystallite sizes and sizes' distribution are determined by using the XRD analysis. The Scherrer's equation, modified Scherrer's method, size–strain (SSP) method, and Williamson–Hall (W–H) method are applied to calculate the values of crystallite sizes. Results reveal average sizes of approximately 30.52 nm, 29.75 nm, 26.75 nm, and 29.51 nm, respectively. Recorded FT-IR spectra confirm the presence of characteristic functional groups and the formation of $ZnSO_4$ NPs. This work contributes to the understanding of sol–gel processing for the synthesis of transition-metal ions'-doped $ZnSO_4$ NPs and their potential applications.

У цій роботі ми повідомляємо про успішну синтезу наночастинок сульфату Цинку ($ZnSO_4$) з використанням золь–ґель-обробляння. Ацетат Цинку служив прекурсором, тоді як $Co(NO_3)_2$, $Cr(NO_3)_3$ та $Fe(NO_3)_3$ використовувалися для досягнення різних рівнів леґування. Синтеза включала процес гідролізи та застигання з ґелеутворенням із подальшим контрольованим випаровуванням розчинника для полегшення утворення наночастинок $ZnSO_4$. Синтезовані наночастинки $ZnSO_4$ було охарактеризовано за допомогою різних методів, включаючи рентґенівську дифракцію (XRD) та ІЧ-спектроскопію з Фур'є-перетвором (FT-

IR), для підтвердження їхньої кристалічної структури. Для аналізи оптичних властивостей було використано ультрафіолетову й оптичну (UV–Vis) спектрофотометрію, якою виявлено значні зміни в забороненій енергетичній зоні. Було представлено детальну аналізу розмірів кристалітів (*D*). Середні розміри кристалітів і розподіл розмірів було визначено за допомогою рентґенівської дифракційної аналізи. Для розрахунку значень розмірів кристалітів було застосовано рівняння Шеррера, модифікований метод Шеррера, розмірно-деформаційний метод (SSP) та метод Вільямсона–Голла (W–H). Результати показують середні розміри приблизно у 30,52 нм, 29,75 нм, 26,75 нм і 29,51 нм відповідно. Записані ІЧ-спектри з використанням Фур'є-перетвору підтверджують наявність характерних функціональних груп та утворення наночастинок $ZnSO_4$. Ця робота сприяє розумінню золь–ґель-обробляння у синтезі наночастинок $ZnSO_4$, леґованих йонами перехідних металів, та їхнього потенційного застосування.

Key words: zinc sulphate, transition-metal ions, crystallite sizes, sol–gel processing, doping, band gap.

Ключові слова: сульфат Цинку, йони перехідних металів, розміри кристалітів, золь–ґель-обробляння, леґування, ширина забороненої зони.

(Received 17 March, 2025; in revised form, 15 May, 2025)

1. INTRODUCTION

Nanotechnology is the field of science, which deals with the fabrication of nanoparticles (NPs) in managing their physical and chemical parameters that enhances their usage in various fields with human benefits. Oxide nanoparticles are particles of metal oxides, ranging in sizes from 1 to 100 nanometers, exhibiting unique properties due to their high surface area-to-volume ratio [1–3]. The study of oxide materials' nanoparticles has caught the interest of scientists due to their optical, electrical, magnetic, mechanical, and catalytic properties, which make them practically valuable from a technological standpoint.

Zinc sulphate ($ZnSO_4$) is an inorganic compound that plays an essential role in a variety of industrial, electronics, agricultural, energy, environmental, and medical applications [4, 5]. Zinc sulphate ($ZnSO_4$) nanoparticles, in particular, attracted considerable attention due to their excellent properties and potential applications in drug delivery, sensors and as catalyst. The dimensions of particulate solids are important in achieving the optimum fabrication for effective medicines [6]. The crystallite-sizes' distribution is a very important property of fine-divided systems such as emulsions, aerosols, and powders. Particle-growth process and its influence on the sizes' distribution have been studied for a long time, and general

theories exist [4]. Understanding and controlling particle sizes is crucial for both manufacturing medicine that contains particulate solids and ensuring the medicine effectiveness after administration. The synthesis of nanoparticles can be approached using different methods, each tailored to achieve specific properties and characteristics. For this purpose, various physicochemical methods are used. Here, there is an overview of some commonly used synthesis methods: sol–gel processing [7, 8], co-precipitation method [9], hydrothermal synthesis [10], green synthesis [11, 12], laser ablation [13], and solid-state reactions [14]. The sol–gel processing has emerged as a versatile method for synthesizing $ZnSO_4$ NPs with controlled morphology and composition, enabling a wide range of applications in different fields.

Doping of oxide nanoparticles is a process, where impurities are intentionally added to an oxide material to modify its electrical, optical, and structural properties. Doping of $ZnSO_4$ with transition-metal ions such as Co^{2+}, Fe^{3+} and Cr^{3+} can significantly enhance its functional properties. The incorporation of these metal ions can lead to changes in the electronic structure and charge-carriers' dynamics, making the doped $ZnSO_4$ NPs particularly interesting for advanced applications. The influence of doping on crystal size in $ZnSO_4$ is a complex phenomenon, and it can vary depending on several factors, including type of dopant, dopant concentration, synthesis conditions, and lattice strain. In summary, doping can have a significant impact on the crystallite size of $ZnSO_4$, and this effect can vary. Analysing of crystallite sizes and strain are crucial in materials science, and several techniques are available such as Scherrer's equation [18, 19], modified Scherrer's method [20], size–strain (SSP) method [21–24], and Williamson–Hall (W–H) method [25–28]. The optical band gap (E_g) is the energy difference between the valence band (VB) and the conduction band (CB), which governs the absorption and emission of light in a material. The determination of the optical band gap is a fundamental aspect of understanding the electronic properties of materials. One effective method for calculating the optical band gap is through the Tauc's law [29].

Our paper is organized as follows. In the first part, we present the sol–gel synthesis of Co-, Cr- and Fe-doped $ZnSO_4$ NPs and their characterization. Detailed analysis of crystallite sizes is discussed in the second part of this study.

2. EXPERIMENTAL DETAILS

2.1. Synthesis of Samples

Zinc acetate ($Zn(CH_3COO)_2{\cdot}2H_2O$, 99.99%), sodium hydroxide (NaOH),

sodium sulphide ($Na_2S{\cdot}9H_2O$, 99.99%), iron nitrate ($Fe(NO_3)_3$, 99.99%), cobalt nitrate ($Co(NO_3)_2$, 99.99%) and chromium nitrate ($Cr(NO_3)_3$, 99.99%) were purchased from Sigma-Aldrich, USA. Distilled water and citric acid ($C_6H_8O_7{\cdot}H_2O$) were used as solvent and stabilizer, respectively. In order to synthesize a clear solution of $ZnSO_4$ NPs, the sol–gel method was used. $ZnSO_4$ NPs are typically fabricate by dissolving 14 g of $Zn(CH_3COO)_2{\cdot}2H_2O$ and 50 g of $Na_2S{\cdot}9H_2O$ in 150 mL of distilled water and stirring the mixture for 6 h at room temperature, using a magnetic stirrer. NaOH solution (8 g of NaOH dissolved in 15 mL of distilled water) was added dropwise to the above solution. To obtain a stable solution, a small amount of citric acid was added. For the synthesis of Co-, Fe- and Cr-doped $ZnSO_4$ NPs, 0.04 g of each impurity was added to $ZnSO_4$ sample, and the same procedure was repeated. The suspended particles were formed that clearly shows the formation of $ZnSO_4$ NPs. Then, the washed solution was dried at 100°C for 24 h and calcined at 600°C for 5 h. The reaction corresponding to the synthesis of $ZnSO_4$ NPs can be represented as follows:

$$Zn(CH_3COO)_2{\cdot}2H_2O + Na_2S{\cdot}9H_2O \rightarrow ZnSO_4 + 2NaCH_3COO + 11H_2O.$$

2.2. Materials Characterizations

The structural parameters of $ZnSO_4$ NPs were determined by using the MiniFlex 600W powder diffractometer with CuK_α radiation ($\lambda = 1.54$ Å) in the range from 3 to 90 degrees; UV–Vis transmittance spectra were measured on a UV-1650-PC, SHIMADZU double beam spectrophotometer. Fourier-transform infrared spectroscopy (FT-IR) spectra were recorded by using the Alpha Bruker FT-IR spectrometer.

3. RESULTS AND DISCUSSION

3.1. XRD Analysis

X-ray diffraction is an effective technique employed to characterize the crystalline structure of materials. These measurements were carried out for pure $ZnSO_4$ and Fe-, Co- and Cr-doped $ZnSO_4$ samples. Figure 1 illustrates the $ZnSO_4$-NPs' XRD patterns, which were calcined at 600°C for five hours. The XRD patterns display several diffraction peaks indicating a good quality of synthesized NPs. In particular, there are eleven distinct peaks at 21.06° (111), 23.37° (200), 32.57° (100), 35.09° (220), 41.46° (311), 42.90° (222), 52.02° (400), 57.08° (024), 61.57° (024), 64.46° (422) and 67.94° (511) in

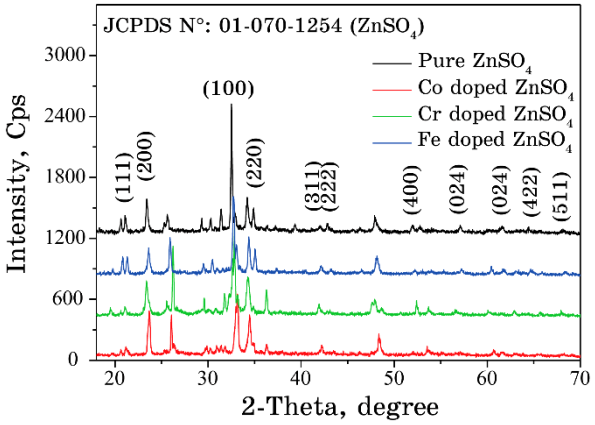

Fig. 1. XRD pattern of pure $ZnSO_4$ and Co, Cr, and Fe-doped $ZnSO_4$ NPs.

2θ-scale. A comparison with the Joint Committee Powder Diffraction Standard card of $ZnSO_4$ indicates that the XRD patterns are consistent with JCPDS No: 01-070-1254. This confirms the formation of a cubic phase of $ZnSO_4$ with the set of lattice parameters: $a = 7.176$ Å, $V_{cell} = 369.528$ Å^3, and the space group F_{23} [30].

Some broad peaks can be attributed to the reflection of quantum confinement effect due to the nanometer sizes of the synthesized NPs. There are three additional peaks, which may correspond to some impurities or defects within the $ZnSO_4$ lattice. The XRD patterns of transition-metal ions'-doped samples are identical to that of the pure one, because of the similarity in ionic radii between these elements: Zn^{2+} (74 pm), Fe^{3+} (63 pm), Co^{2+} (72 pm) and Cr^{3+} (61 pm).

3.2. Crystallite Size Determination

The XRD method is typically used for determining the crystallite sizes and shape. For $ZnSO_4$ nanoparticles, the average mean size was calculated, using the Scherrer's equation [31]. Principally, Scherrer's equation can be described as

$$D = \frac{0.9\lambda}{\beta \cos\theta}, \qquad (1)$$

where D denotes the mean crystallite size, θ refers to the Bragg diffraction angle, λ denotes the x-ray wavelength (1.546 Å), and β presents the *FWHM* of the selected peaks. The crystallite sizes of pure $ZnSO_4$, Co-doped $ZnSO_4$, Cr-doped $ZnSO_4$, and Fe-doped $ZnSO_4$ NPs were found to be 36.968 nm, 23.881 nm, 31.387 nm, and 31.423 nm, respectively.

The second method used to minimize errors in determining the crystallite size is the modified Scherrer's equation [32], which can be expressed as follows:

$$\ln(\beta) = \ln\left(\frac{0.9\lambda}{D\cos\theta}\right) = \ln\left(\frac{0.9\lambda}{D}\right) + \ln\left(\frac{1}{\cos\theta}\right), \tag{2}$$

Figure 2 illustrates the plot of ln(β) against ln(1/cosθ); the crystallite size (D) was calculated from the intercept ln(0.9λ/D).

In order to obtain an excellent precise determination of size–strain parameters, the size–strain plot (SSP) method has been used. This method considers the x-ray diffraction peak profile as a combination of both Lorentzian (crystallite size) and Gaussian (strain) functions [33, 35]. The SSP is calculated using the following equation [36]:

$$\left(d_{hkl}\beta\cos\theta\right)^2 = \frac{0.9\lambda}{D}\left(d_{hkl}^2\beta\cos\theta\right) + \left(\frac{\varepsilon}{2}\right)^2. \tag{3}$$

The plot of $\left(d_{hkl}\beta\cos\theta\right)^2$ *versus* $\left(d_{hkl}^I\beta\cos\theta\right)$ is shown in Fig. 3. Using the linear fit of data, the crystallite sizes were obtained from

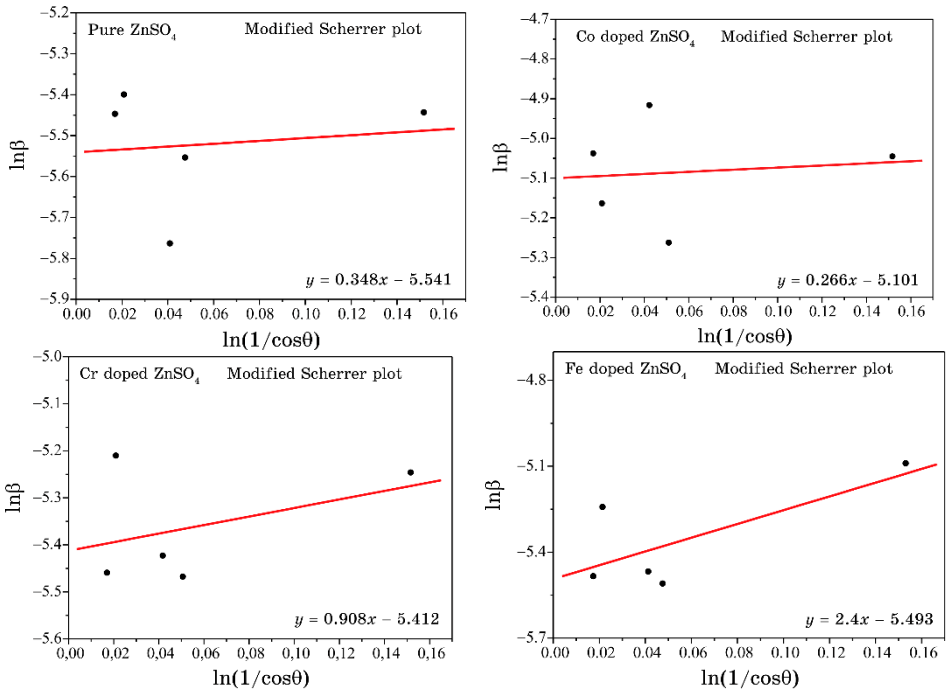

Fig. 2. Modified Scherrer's plot for $ZnSO_4$ NPs.

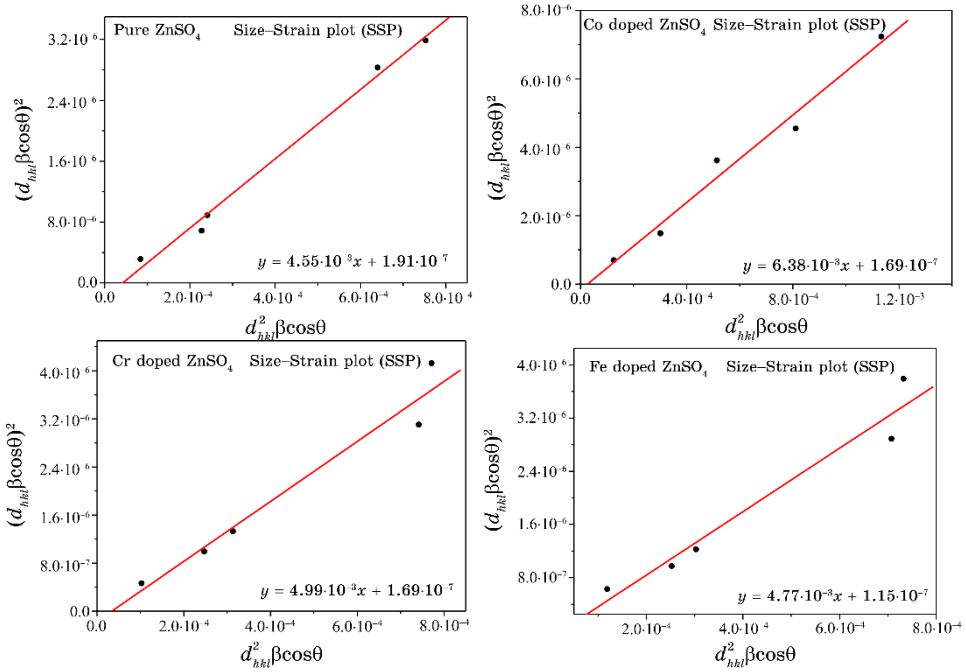

Fig. 3. Size–strain plot for $ZnSO_4$ NPs.

the slope of the line; the strain value was estimated from the square root of the *y*-intercept.

From the Williamson–Hall (W–H) plot [37, 38], the broadening of diffraction peaks can be expressed as

$$\beta_{hkl} = \beta_{size} + \beta_{strain}. \tag{4}$$

Observed β_{hkl} as a function of microstrain (ε) can be given by

$$\beta_{hkl} \cos\theta = \frac{k\lambda}{D} + 4\varepsilon \sin\theta\,. \tag{5}$$

The plot of $\beta_{hkl}\cos\theta$ *vs.* $4\sin\theta$ has been represented in Fig. 4. The strain was calculated from the slope, and the intercept gives the values of crystallite size.

Dislocation density (δ) is an important parameter in materials science that measures the number of dislocations within the material microstructure. Dislocations are line defects in the crystal lattice, which can have a substantial impact on mechanical properties, including strength and ductility. This parameter (δ) is defined as the cumulative length of dislocation lines per unit volume of the material and is usually expressed in units of m^{-2}. The dislocation

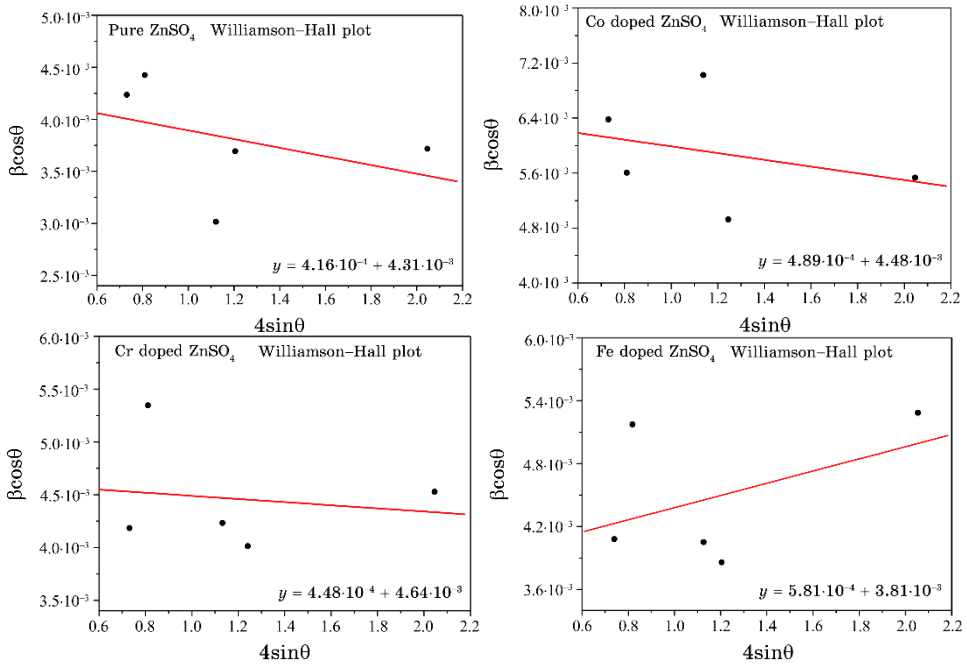

Fig. 4. The Williamson–Hall plot for $ZnSO_4$ NPs.

TABLE 1. Comparison of crystallite sizes, microstrain and dislocation density in $ZnSO_4$ NPs.

Samples	Scherrer's equation	Modified Scherrer's plot	Size–strain plot (SSP)		Williamson–Hall plot, W-HP		δ, line/m^2·10^{14}
	D, nm	*D*, nm	*D*, nm	ε·10^{-4}	*D*, nm	ε·10^{-4}	
Pure $ZnSO_4$	36.968	34.736	30.395	8.74	32.157	4.16	07.31
Co doped $ZnSO_4$	23.881	22.391	21.724	8.24	21.388	4.89	17.53
Cr doped $ZnSO_4$	31.387	30.528	27.775	8.22	29.871	1.48	10.15
Fe doped $ZnSO_4$	31.423	33.158	29.056	6.78	36.473	5.82	10.11

density, δ, was determined, using the formula provided in Ref. [39]:

$$\delta = \frac{1}{D^2}, \tag{6}$$

and together with the resulting values is presented in Table 1. Re-

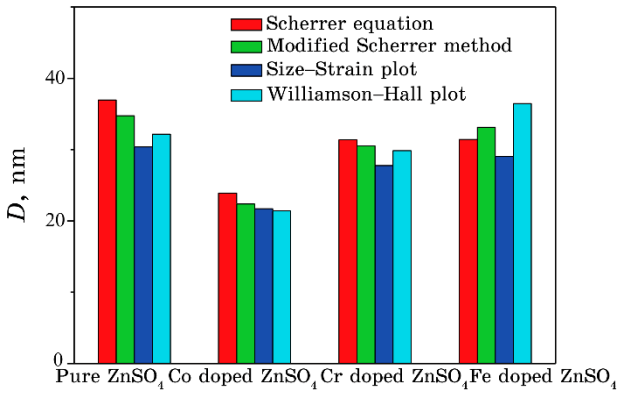

Fig. 5. Crystallite size *vs.* type of dopant.

sults obtained by means of all methods are presented in Table 1 too.

Different values of crystallites' size have been observed for the set of nanoparticles; the presence of particles of different morphology and size can be attributed to the type of dopant. The flow and compaction properties have been controlled by the size of the particles. Figure 5 shows the particles'-size distribution as a function of type of dopant. It is clearly seen that the small values of crystallites' size were observed for the Co-doped $ZnSO_4$ sample.

3.3. FT-IR Spectroscopy

Fourier transform infrared (FT-IR) spectroscopy is an important analytical method employed to identify functional groups, chemical bonds, and identifying compounds [40]. The FT-IR transmittance spectra of pure $ZnSO_4$ and Co-, Cr- and Fe-doped $ZnSO_4$ NPs were obtained in the transmittance mode at room temperature, using the Alpha Bruker FT-IR spectrometer in the range of 400–4000 cm^{-1}. Here, the KBr pellet technique was used. Figure 6 shows the FT-IR spectra of pure $ZnSO_4$ and Co-, Cr- and Fe-doped $ZnSO_4$ NPs. These last ones measure the absorption of infrared light by a sample, which causes molecular vibrations. The symmetric stretching mode of water molecule (O–H) is characterized by the presence of broad vibrational band at 3443 cm^{-1} in the FT-IR spectra. The sharp band at 1626 cm^{-1} is attributed to the bending mode of CO_2 molecules. The bands located at 987 and 1405 cm^{-1} correspond to stretching vibrations in the sulphate SO_4^{-2} ions [41]. The bands located at 558, 944 and 625 cm^{-1} may indicate the presence of Co–O [42], Cr–O [43] and Fe–O [44] stretching vibrations, respectively. This one confirms the successful incorporation of metallic ions in $ZnSO_4$ NPs.

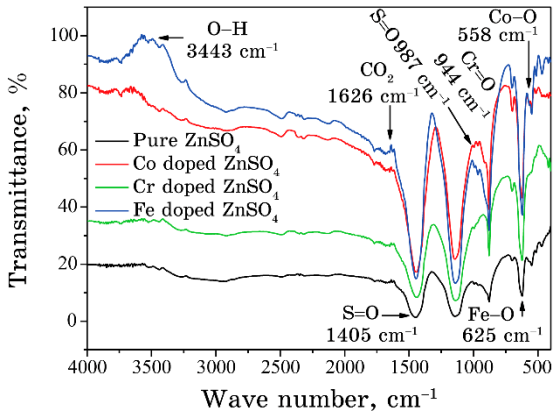

Fig. 6. FT-IR spectra of pure $ZnSO_4$ and Co-, Cr-, and Fe-doped $ZnSO_4$ NPs.

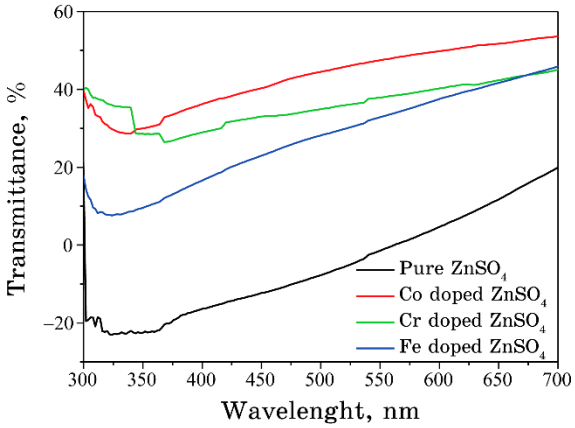

Fig. 7. UV–visible transmittance spectra for pure $ZnSO_4$ and Co-, Cr-, and Fe-doped $ZnSO_4$.

3.4. Optical Band Gap Analysis with UV–Visible Spectrum

UV–visible transmittance spectra for the newly prepared $ZnSO_4$ nanoparticles are depicted in Fig. 7. These spectra were recorded within the range of 200–800 nm. All samples show a weak absorption peaks near 320 nm due to the band π–π^* electronic transition and to the surface-plasmon resonance of the pure $ZnSO_4$ sample.

Additionally, optical band-gap values ($E_{opt.}$) for direct transition were estimated, using the absorption coefficient (α). In ineffective thickness method (ITM), m characterizes the indirect allowed and forbidden transitions, direct allowed and forbidden ones and has values of 1/2, 3/2, 2 and 3, respectively. In this study, we are in-

teresting in the direct transition ($m = 2$). Tauc's plot is a graphical method used to determine the optical band gap of semiconductor materials. This last relates the absorption coefficient (α) of a material to the energy of the incident light ($h\nu$). The classic Tauc's approach was used to calculate band-gap energy of the samples, according to Eq. (9) as shown below [45, 46]:

$$(\alpha h\nu)^2 = A\left(h\nu - E_g\right), \tag{9}$$

where α is the absorbance coefficient, h is the Planck constant, A is the absorption constant for a direct transition, $h\nu$ is the absorption energy, and E_g represents the band gap.

The intercepts of lines with x-axis gives $E_{opt.}$ values. Similarly, for direct transition ($m = 2$), relations between $(\alpha h\nu)^2$ *vs.* $h\nu$ for different synthesized $ZnSO_4$ NPs were plotted (Fig. 8) and values of $E_{opt.}$ were obtained from lines' intercepts with x-axis. Values of optical band gap ($E_{opt.}$) for direct transition were listed in Table 2. In case of the direct transitions, $E_{opt.}$ values are ranged between 1.856 eV and 2.821 eV. When Cr^{3+} ions are introduced into the

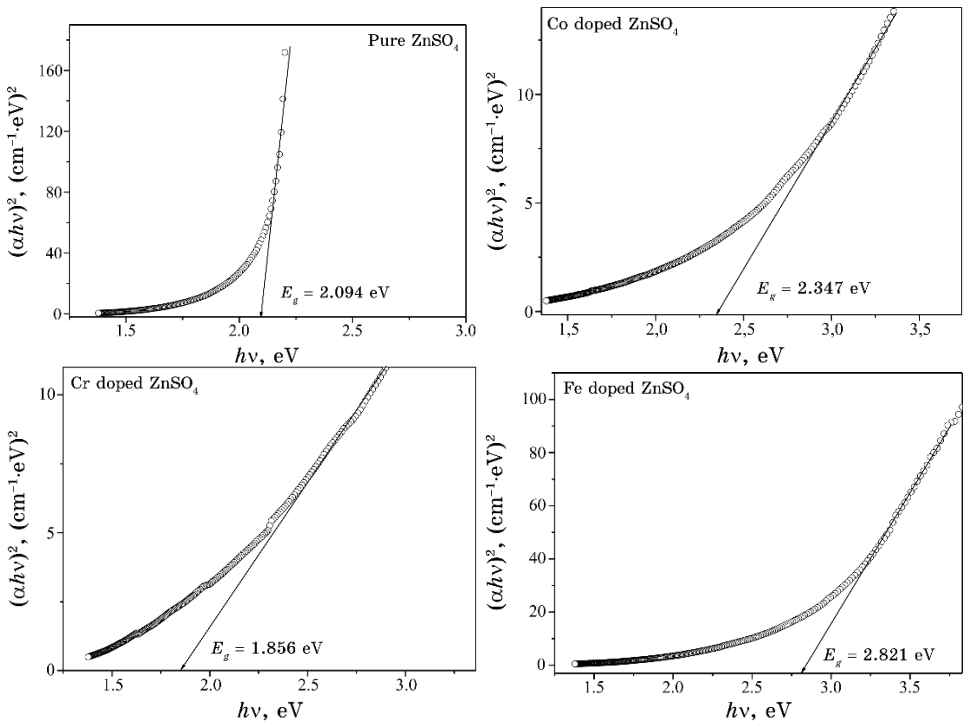

Fig. 8. Plot of $(\alpha h\nu)^2$ *vs.* $h\nu$ from the UV–visible transmittance for pure $ZnSO_4$ and Co-, Cr-, and Fe-doped $ZnSO_4$ NPs.

TABLE 2. Optical band gap (E_g) and refractive index (n) values.

Samples	E_g, eV	Refractive index (n)
Pure $ZnSO_4$	2.094	1.471
Co doped $ZnSO_4$	2.347	1.649
Cr doped $ZnSO_4$	1.856	1.304
Fe doped $ZnSO_4$	2.821	1.982

$ZnSO_4$ matrix, it can create localized energy state within the band gap. These states can facilitate electron transitions, effectively reducing the energy required for an electron to jump from the valence band to the conduction band, thus, decreasing the optical-band gap. The presence of these ions can increase the concentration of charge carriers (electrons or holes) in the materials. This increase can lead to enhanced conductivity and a reduction in the effective band gap due to more available states for electron excitation. Fe^{3+} and Co^{3+} ions may introduce additional energy levels or modify the electronic structure of $ZnSO_4$. If iron is present in higher oxidation states, it can lead to an increase in the effective energy required for electron transitions, thus, widening the band gap. Doping with Fe^{3+} and Co^{3+} ions can lead to increased localization of charge carriers. This localization can create a scenario, where the electron transitions from the valence band to higher energy state require more energy, contributing to a larger band gap.

Nanoparticles, particularly semiconducting or metallic ones, have a refractive index (n) that determines these-materials' interaction with light impacting light scattering, emission and absorption. This index (n) is important in designing some devices as the optical ones, influencing transparency and responding to external stimulation. Refractive index (n) is calculated, using the relation [47]

$$\frac{n^2-1}{n^2+2} = 1 - \sqrt{\frac{E_{opt.}}{20}}\,.$$

It is ranged from 1.304 to 1.982 for direct transitions as listed in Table 2 reflecting the high transparency of nanoparticles across both the visible and UV spectrum, which make it for photodetectors and solar cells as an ideal candidate. These values reflect the material efficiency in bending photons that is desired for optical devices.

4. CONCLUSIONS

In summary, zinc sulphate ($ZnSO_4$) NPs were successfully synthesized, using the sol–gel processing. Four samples have been synthe-

sized: pure $ZnSO_4$, Co-doped $ZnSO_4$, Cr-doped $ZnSO_4$ and Fe-doped $ZnSO_4$. Various advanced characterisation techniques were employed, including x-ray diffraction (XRD), Fourier transform infrared (FT-IR) spectroscopy and UV–visible spectroscopy. These last provided a detailed understanding of the crystalline structure, vibrational modes and optical properties of the synthesized $ZnSO_4$ NPs. FT-IR spectra confirm the presence of all functional groups and demonstrated the successful synthesis of $ZnSO_4$ NPs. X-ray diffraction analysis (XRD) confirms the crystalline (cubic) nature of the $ZnSO_4$ NPs. Scherrer's equation, modified Scherrer's method, size–strain (SSP) method and the Williamson–Hall (W–H) method were used to examine the crystallite sizes and intrinsic strain of our samples based on the XRD peaks. A comprehensive comparison of average particle sizes obtained from these models was conducted and revealing an average sizes of approximately 30.52 nm, 29.75 nm, 26.75 nm and 29.51 nm, respectively. The dislocation density was investigated; this parameter was estimated from $7.31 \cdot 10^{14}$ to $10.11 \cdot 10^{14}$ line/m^2. Analysis of UV–Vis transmittance spectra indicates an apparent increase of optical-band gap from 2.094 eV (pure $ZnSO_4$) to 2.347 eV (Co-doped $ZnSO_4$) and 2.821 eV (Fe-doped $ZnSO_4$). Doping of $ZnSO_4$ with Cr ions cased the decreasing of the band-gap value from 2.094 eV to 1.856 eV. The study suggests that $ZnSO_4$ NPs doped with transition-metal ions such as Co^{3+}, Cr^{3+} and Fe^{3+} are the potential candidate to fabricate semiconductor nanooptical wide-band gap device based on their augmented band gap.

REFERENCES

1. P. Madhuri Santhoshi, P. Tirupathi Rao, K. Vasudha, Esub Basha, Deepti Bhargava, T. K. Visweswara Rao, P. S. S. S. Sai Kiran, and R. K. Ramachandra, *J. Mol. Struct.*, **1262**: 132944 (2022); https://doi.org/10.1016/j.molstruc.2022.132944
2. Angie Xiomara Vesga, María Fernanda Cuentas, and Alberto Ricardo Albis Arrieta, *Heliyon*, **10**, Iss. 12: 33117 (2024); https://doi.org/10.1016/j.heliyon.2024.e33117
3. Qi Zhang, Junchang Liu, Hongying Xia, Yingjie Xu, and Libo Zhang, *Ultrason. Sonochem.*, **102**: 106748 (2024); https://doi.org/10.1016/j.ultsonch.2023.106748
4. Sidi Ye, Siqi Sheng, Hua Yao, Qian Chen, Lili Meng, and Yangyi Yang, *J. Energy Storage*, **100**: 113674 (2024); https://doi.org/10.1016/j.est.2024.113674
5. Zihe Wei, Xuehua Wang, Ting Zhu, Ping Hu, Liqiang Mai, and Liang Zhou, *Chin. Chem. Lett.*, **35**, Iss. 1: 108421 (2024); https://doi.org/10.1016/j.cclet.2023.108421
6. Yashwant Singh, Shakti Nath Tripathi, Praveen Pandey, Arpita Tripathi, Namira Arif, Vaishali Yadav, Shweta Gaur, and Devendra K. Chauhan, *Ind.*

Crop. Prod., **212**: 118378 (2024); https://doi.org/10.1016/j.indcrop.2024.118378
7. Zhijie Li, Wenzhong Shen, Limei Fang, and Xiaotao Zu, *J. Alloys Compd.*, **463**, Iss. 1–2: 129 (2008); https://doi.org/10.1016/j.jallcom.2007.09.075
8. Vishwajeet V. Aherkar, Sidhaling B. Bhairunagi, Muddsar L. Gaur, and Rekha M. Ovhal, *Optik*, **302**: 171720 (2024); https://doi.org/10.1016/j.ijleo.2024.171720
9. N. Manivannan, B. Chandar Shekar, C. K. Senthil Kumaran, P. Matheswaran, B. Gokul, and M. Mohammed Ibrahim, *Mater. Today: Proc.*, **47**, Pt. 9: 1741 (2021); https://doi.org/10.1016/j.matpr.2021.02.325
10. E. Muhammed Jubeer, M. Aslam Manthrammel, P. A. Subha, Mohd Shkir, K. P. Biju, Meenakshi Verma, and S. AlFaify, *Radiat. Phys. Chem.*, **225**: 112154 (2024); https://doi.org/10.1016/j.radphyschem.2024.112154
11. G. Sangeetha, S. Rajeshwari, and R. Venckatesh, *Mater. Res. Bull.*, **46**: 2560 (2011); https://doi.org/10.1016/j.materresbull.2011.07.046
12 Nurul Ain Samat and Roslan Md Nor, *Ceram. Int.*, **39**, Supplement 1: S545 (2013); https://doi.org/10.1016/j.ceramint.2012.10.132
13. Lanhui Wang, Ji Ren, Kui Lin, Yanxu Chang, Lifeng Han, and Fei Tian, *J. Alloys Compd.*, **803**: 844 (2019); https://doi.org/10.1016/j.jallcom.2019.06.325
14. Xiaoxia Li, Zhong Chen, Zhiyong Yu, Xinyang Huang, Quanmao Yu, Shuzhen Wang, Zheming Wang, Dongqin Wan, and Maohua Luo, *J. Lumin.*, **190**: 364 (2017); https://doi.org/10.1016/j.jlumin.2017.05.076
15. Mélanie Auffan, Jérôme Rose, Jean-Yves Bottero, Gregory V. Lowry, Jean-Pierre Jolivet, and Mark R. Wiesner, *Nat. Nanotechnol.*, **4**: 634 (2009); https://doi.org/10.1038/nnano.2009.242
16. Kannan Badri Narayanan and Natarajan Sakthivel, *Adv. Colloid Interface Sci.*, **156**: Iss. 1–2: 1 (2010); https://doi.org/10.1016/j.cis.2010.02.001
17. Tammineni Venkata Surendra, Selvaraj Mohana Roopan, and Maksudur R. Khan, *Mater. Today: Proc.*, **35**, Iss. 4: 2823 (2019); https://doi.org/10.1002/btpr.2823
18. A. Patterson, *Phys. Rev.*, **56**: 978 (1939); https://doi.org/10.1103/PhysRev.56.978
19. S. Anbarasu, S. Ilangovan, V. S. Nagarethinam, J. Srivind, S. Balamurugan, M. Suganya, and A. R. Balu, *Nano-Struct. Nano-Objects*, **17**: 67 (2019); https://doi.org/10.1016/j.nano.2018.11.013
20. Mehjabeen Khan, Ashutosh Mishra, Jyoti Shukla, and Pradeep Sharma, *AIP Conf. Proc.*, **2100**: 020138 (2019); https://doi.org/10.1063/1.5098692
21. Debojyoti Nath, Fouran Singh, and Ratan Das, *Mater. Chem. Phys.*, **239**: 122021 (2020); https://doi.org/10.1016/j.matchemphys.2019.122021
22. M. A. Tagliente and M. Massaro, *Nucl. Instrum. Methods Phys. Res. Sect. B: Beam Interact. Mater. Atoms*, **266**, Iss. 7: 1055 (2008); https://doi.org/10.1016/j.nimb.2008.02.036
23. A. Khorsand Zak, R. Razali, W. H. Abd Majid, and Majid Darroudi, *Int. J. Nanomed.*, **6**: 1399 (2011); https://doi.org/10.2147/IJN.S19693
24. V. Mote, Y. Purushotham, and B. Dole, *J. Theor. Appl. Phys.*, **6**, No. 1: 1 (2012); https://doi.org/10.1186/2251-7235-6-6
25. R. Das and S. Sarkar, *Curr. Sci.*, **109**: 775 (2015).
26. A. R. Stokes and A. J. C. Wilson, *Proc. Phys. Soc.*, **56**, No. 3: 174 (1944);

https://doi.org/10.1088/0959-5309/56/3/304
27. W. H. Hall, *Proc. Phys. Soc. Sect. A*, **62**, No. 11: 741 (1949); https://doi.org/10.1088/0370-1298/62/11/110
28. A. Khorsand Zak, W. H. Abd. Majid, M. E. Abrishami, and Ramin Yousefi, *Solid State Sci.*, **13**: 251 (2011); https://doi.org/10.1016/j.solidstatesciences.2010.11.024
29. J. Tauc, *Mater. Res. Bull.*, **3**: Iss. 1: 37 (1968); https://doi.org/10.1016/0025-5408(68)90023-8
30. M. Spiess and R. Gruehn, *Naturwissenschaften*, **65**: 594 (1978); https://doi.org/10.1007/BF00364914
31. See Ref. [18].
32. See Ref. [20].
33. Debojyoti Nath, Fouran Singh, and Ratan Das , *Mater. Chem. Phys.*, **239**: 122021 (2020); https://doi.org/10.1016/j.matchemphys.2019.122021
34. See Ref. [22].
35. See Ref. [23].
36. See Ref. [24].
37. See Ref. [27].
38. G. K. Williamson and W. H. Hall, *Acta Metall.*, **1**, Iss. 1: 22 (1953); https://doi.org/10.1016/0001-6160(53)90006-6
39. G. K. Williamson and R. E. Smallman, *Philos. Mag.*, **1**, Iss. 1: 34 (1956); https://doi.org/10.1080/14786435608238074
40. C. Alosious Gonsago, Helen Merina Albert, J. Karthikeyan, P. Sagayaraj, and A. Joseph Arul Pragasam, *Mat. Res. Bull.*, **47**, Iss. 7: 1648 (2012); https://doi.org/10.1016/j.materresbull.2012.03.061
41. Helen Merina Albert, T. Lohitha, Karthik Alagarsamy, C. Alosious Gonsago, and Vinita Vishwakarma, *Mater. Today: Proc.*, **47**, Pt. 4: 1030 (2021); https://doi.org/10.1016/j.matpr.2021.06.124
42. A. A. E. Aboelazm, A. Gomaa, M. Ali, and K. F. Chong, *Chem. Adv. Mater.*, **3**, Iss. 4: 67 (2018); https://doi.org/10.22034/cam.2018.123899.1080
43. Mahendra Kumar Trivedi, Rama Mohan Tallapragada, Alice Branton, Dahryn Trivedi, Gopal Nayak, Omprakash Latiyal, and Snehasis Jana, *J. Powder Metall. Min.*, **5**, Iss. 4: 1 (2015); http://dx.doi.org/10.4172/2090-4568.1000136
44. K. Winiarczyk, W. Gac, M. Goral-Kowalczyk, and Z. Surowiec, *Hyperfine Interact.*, **242**: Article No. 48 (2021); https://doi.org/10.1007/s10751-021-01768-w
45. D. R. Sahu, *Microelectron. J.*, **38**, Iss. 12: 1252 (2007); https://doi.org/10.1016/j.mejo.2007.09.025
46. A. Escobedo-Morales, I. I. Ruiz-López, M. d. Ruiz-Peralta, L. Tepech-Carrillo, M. Sánchez-Cantú, and J. E. Moreno-Orea, *Heliyon*, **5**, Iss. 4: 01505 (2019); https://doi.org/10.1016/j.heliyon.2019.e01505
47. S. Lakshimi, S. Rao, G. Ramadevudu, and M. Shareefuddin, *Int. J. Eng. Sci. Tech.*, **4**, Iss. 4: 25 (2012); https://doi.org/10.4314/ijest.v4i4.2